PPK PROCESSING TO BOOST UAS ACCURACY IN CADASTRAL MAPPING

V. E. Oniga[1,2], L. Morelli[3,4], M. Macovei[1], C. Chirila[1], A. I. Breaban[5], F. Remondino[3], P. Sestraș[6]

[1] Department of Terrestrial Measurements and Cadastre, Faculty of Hydrotechnical Engineering, Geodesy and Environmental Engineering, „Gheorghe Asachi" Technical University of Iasi, Professor Dimitrie Mangeron Boulevard 67, 700050, Iasi, Romania – <valeria-ersilia.oniga><mihaela.macovei><constantin.chirila>@academic.tuiasi.ro

[2] Romanian Society of Photogrammetry and Remote Sensing, Lacul Tei Blvd. 124, 020396, Bucharest, Romania – chair.srft@srft.ro

[3] 3D Optical Metrology (3DOM) unit, Bruno Kessler Foundation (FBK), Trento, Italy – <lmorelli><remondino>@fbk.eu

[4] Dept. of Civil, Environmental and Mechanical Engineering (DICAM), University of Trento, Italy

[5] Department of Terrestrial Measurements and Cadastre, Faculty of Geodesy, Technical University of Civil Engineering Bucharest, Teiul Doamnei Street, 023585, Bucharest, Romania – anaioana2004@yahoo.co.uk

[6] Department of Land Measurements and Cadastre, Faculty of Civil Engineering, Technical University of Cluj-Napoca, 400020 Cluj-Napoca, Romania – psestras@mail.utcluj.ro

Commission II

KEY WORDS: UAS photogrammetry, GNSS, PPK, DJI Phantom 4 Pro v2, cadastral mapping, accuracy, TeoKIT

ABSTRACT:
Unmanned Aerial Systems (UAS) are increasingly used in different applications, including 3D urban modelling, cadastral mapping, urban planning, GIS information system and other fields because of their advantages. As a consequence, UAS equipment is constantly developed to provide more accurate results in a more reliable mode. This paper aims to evaluate the performances of a low-cost UAS system, namely DJI Phantom 4 Pro v2 equipped with a TeoKIT GNSS PPK (post-processing kinematic) module for cadastral mapping purposes. Two fights (oblique and nadir) over a residential area at 60 m height were performed and some 100 ground points were used to derive RMSE accuracies. Comparison between GNSS-aided with PPK processing and indirect georeferencing processes are performed. Given a mobile laser scanner (MLS) point cloud as ground truth, comparison with UAS point clouds and manually digitized features are also performed and reported.

1. INTRODUCTION

Unmanned aerial systems (UASs) have been extensively adopted for surveying purposes due to their data acquisition speed, as well as their unrestrained mobility useful to acquire a robust photogrammetric block. Images are typically processed with an automated Structure-from-Motion (SfM) pipeline that provides a 3D reconstruction known only up to a scale factor (Micheletti et al., 2015; Oniga et al., 2020). Ground Control Points (GCPs), which are usually surveyed with GNSS or total stations, are commonly employed to scale and/or georeference the resulting 3D model (Oniga et al., 2020), and included into the bundle block adjustment (BBA) algorithm as additional constraints. While this approach is widely used in UAS surveys, it can be exceedingly time-consuming. Furthermore, evenly distributed and highly accurate GCPs across the study area can be challenging, particularly in areas with rugged terrain, steep slopes, dense vegetation or inaccessible areas (Tomaštík et al., 2019; Nesbit et al., 2022).
In recent years, significant efforts have been made to eliminate the use of GCPs in photogrammetric applications, particularly in UAS surveys. This has been achieved by replacing topographic campaigns with high-quality Global Navigation Satellite System (GNSS) receivers mounted directly on the UAS platforms (Cucci et al., 2017; Ioli et al., 2021), integrating angular attitude measurements from accelerometers and gyroscopes (Stöcker et al., 2017), or employing other sensor fusion techniques (Negru et al., 2023). It is important to note that an efficient synchronisation between different sensors is essential due to the high speed of the UAS during surveys (Ekaso et al., 2020; Pargieła, 2023).
Few studies have aimed to eliminate the need for GCPs in ground-based surveys, particularly for applications where UAS usage is not feasible due to regulatory restrictions, safety concerns, or security issues (Forlani et al., 2014; Morelli et al., 2022; Nesbit et al., 2022). Most works on UAS GNSS-aided photogrammetry without GCPs, improperly referred to as direct-georeferencing (Xiang and Tian, 2011; Granshaw, 2016; Benassi et al., 2017), utilise an on board GNSS antenna to georeference the photogrammetric image block. Generally, the integration of oblique images significantly improves the camera calibration and the overall object space accuracy (Teppati et al., 2020; Zeybek, 2021). In the scenario of only nadiral images, while on the horizontal accuracy literature results are quite coherent, showing that 2-3 cm accuracy is reachable, on the vertical direction results are more inhomogeneous. E.g., Teppati et al. (2020) assesses that if only nadiral images and PPK COPs are used, accuracy from few decimeters to metres is reached at GSD of 1.5cm/px. In case of only nadiral images a single GCP is needed to significantly increase the accuracy, but the accuracy is still of few decimeters. If oblique images are added to the nadiral block, no GCPs are needed to reach 3cm total Root Mean Square Error (RMSE) at 1.5cm/px GSDOther studies showed less marked differences between horizontal and vertical errors using only nadir images. Hugenholtz et al. (2016) reached 3 cm of horizontal accuracy, but 12cm as vertical error, suggesting the use of GCPs to obtain the most accurate vertical accuracies. Benassi et al. (2017) showed that the average of the vertical error in their flights varied from 0.8 to 4 GSD. Finally, it is generally preferred PPK to RTK not to rely on online GNSS correction, or to have more control on the data quality.

1.1 Paper contributions

Our paper provides an insight into the use of PPK processing with GNSS hardware for UAS surveys in residential areas, as well as

a comparison of UAS point clouds and terrestrial laser scanner surveys. Therefore, this paper brings three main contributions:

(i) evaluation of PPK processing to georeference UAS image blocks, analysing accuracy's variation in object space by using an incremental number of GCPs (from 0 to 10);
(ii) utilisation of a surveying case study in a rural area, based on the low-cost and high-performance TeoKIT[1] GNSS receiver and antenna;
(iii) comparison of the UAS-based results with those of a mobile terrestrial laser scanner, discussing their advantages and limitations.

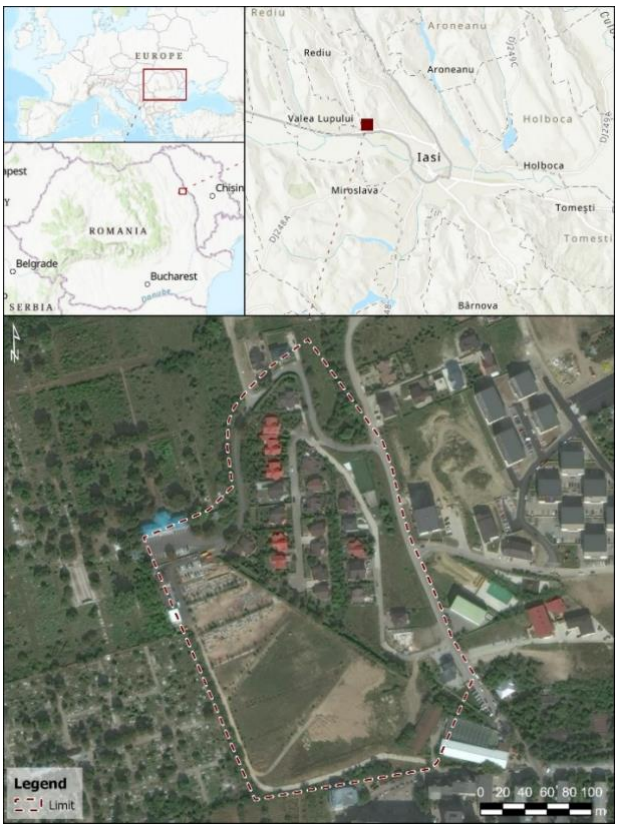

Figure 1. Location of the study area.

2. METHODOLOGY

2.1 Study area

The study area is located near Iasi (Romania), it covers ca 7.2ha with a residential area (houses surrounded by natural and artificial fences, private roads, cemetery, vegetation - Figure 1). According to the Urban General Plan, it is considered an integral part of the Municipality of Iasi, and the site exhibits all the characteristics of a rural area. The results of this study may thus be applied to villages, semi-urban or peri-urban areas in different countries.

The area was surveyed with two UAV flights, one with nadir images and one with an oblique camera view (45 deg).

2.2 Measurement and materialisation of GCPs

Prior to conducting the UAS flights, a set of 100 GCPs were grounded with wooden sticks and metallic bolts or using plexiglass plates featuring two black and orange triangles, respectively, measuring 3 mm thick and 40 cm × 40 cm in dimension (Figure 2a-b). GCPs were distributed uniformly over the study area (Figure 2c). To ensure a high level of accuracy, the GCP positions were surveyed with a multi-band Emlid Reach RS2 GNSS receiver with centimetric accuracy using the Romanian Positioning Determination System (ROMPOS) employing GNSS-RTK technology. The GCPs planimetric coordinates were determined in the Romanian national coordinate system "Stereographic on a unique secant plane-1970" (STEREO-70).

Figure 2. GCPs materialisation (a), GCPs marking on the ground (b) and the spatial distribution of the 100 GCPs (c).

Additionally, the ellipsoidal heights were transformed from the ETRS89 European datum into Black Sea-1975 normal heights, which corresponds to the RO Const/NH vertical datum (Dragomir et al., 2011). The TransDatRO software (ver. 4.07) provided by the National Agency for Cadaster and Land Registry (NACLR) was utilised for this transformation. During the processing (Section 3), out of the measured 100 GCPs, only 94 were used, as 6 suffered field displacements.

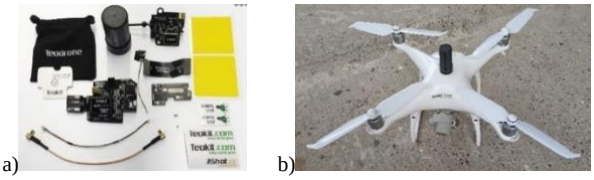

Figure 3. TeoKIT UAV PPK kit (a) and DJI Phantom 4 Pro V2 UAS system with the TeoKIT installed (b).

[1] https://teokit.com/, https://fly.teofly.com/app/

2.3 TeoKIT installation on DJI Phantom 4 Pro V2

The TeoKIT L1/L2 (Figure 3a) is a cost-effective PPK solution for UAS systems. For the presented work, the TeoKIT was integrated with a DJI Phantom 4 Pro v2 UAS (Figure 3b). The TeoKIT components are:
– HX-CH6601A HELIX GNSS antenna (L1/L2), a highly sensitive spiral antenna, centred on the top of the DJI Phantom UAS system (Figure 3b) and able to receive multiple signals (GPS + GLONASS - 15 Hz, GPS + GLONASS + BEIDOU or GALILEO - 10 Hz).
– AGNSS L1/L2 board, a high-performance board for DJI drones.
– Teoboard, an electronic timing board which enables the GNSS signal distribution from the spiral antenna to the GNSS board and DJI GPS module.
– AShot board which sends timemark signal to the GNSS board taking into consideration the camera settings (shutter speed, exposure time).

2.3 Data acquisition using Teodrone

The DJI Phantom 4 Pro v2 integrates a FC6310S digital camera with a 8.8 mm focal length, image size of 5472×3648 pixels and a pixel size of 2.41 µm. The Ground Sample Distance (GSD) of the nadir flight is approximately 1.9 cm (3.2 cm for the oblique dataset). Flight missions were planned using the dedicated Teofly application (https://fly.teofly.com/app/) and the following parameters:
– 10 m/s speed,
– 10 km maximum length of the flight itinerary,
– 500 m maximum distance between waypoints,
– -90^0 (nadir flight), respectively -45^0 (oblique flight) for the camera pitch,
– 80% as front overlap,
– 70% as side overlap,
– 60 m as flight height
– 2 s as image acquisition interval,
– camera shutter speed of 1/1600,
– exposure time of 1/1000.
The Shuttle Radar Topographic Mission (SRTM) open-source Digital Terrain Model was selected as DTM for the flight planning. The flight plan followed a "double grid" option.

(a) (b)

Figure 4. Planned flights with double grid for oblique (a) and nadir (b) images.

The two flight missions were configured and loaded onto the UAS system. The oblique flight took 13 minutes, while the nadiral flight took 14 minutes. As a result of the flights, 591 oblique images and 606 nadiral images were obtained.

2.4 Data acquisition using Mobile Laser Scanner (MLS)

In September 2022, the study area was surveyed using a Trimble MX9 mobile laser scanning (MLS) system (Figure 5a) mounted on top of a car that followed the itinerary displayed in Figure 5b. The MX9 system is equipped with two laser scanners capable of acquiring data at a maximum range of 475 meters for targets with reflectivity greater than 80%, at a rate of 500 scans per second, with a 5 mm accuracy. Additionally, the system has one spherical camera with 30 Mpixel resolution (composed of 6 x 5 megapixel sensors), two side-facing cameras with 12 MPixel resolution and one backward/downward-facing camera with 12 MPixel resolution. These cameras are used for high-density point cloud texturing. The MLS point cloud data has a planimetric accuracy of 2 cm and a vertical accuracy of 5 cm[2]. The scanning process produced a point cloud of ca 192 million points (Figure 5c). The coordinates for the MLS point cloud are in the STEREO-70 coordinate system, while the Z coordinates are in Black Sea-1975 normal heights.

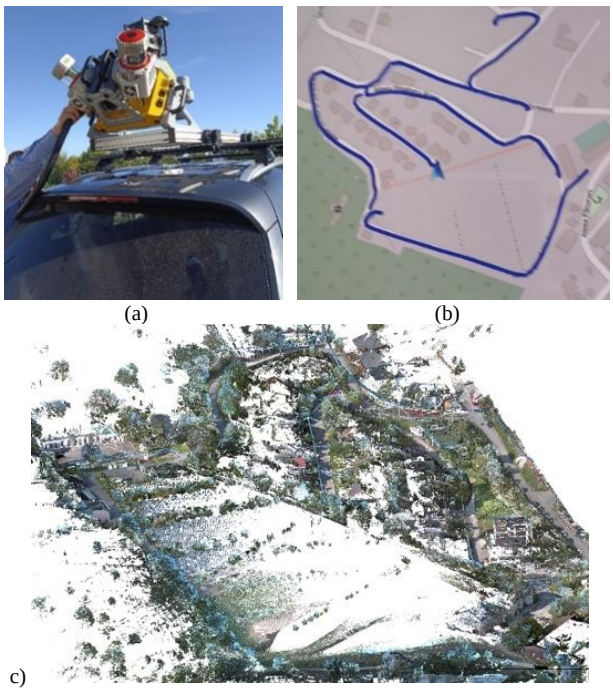

(a) (b)

c)

Figure 5. Trimble MX9 mobile laser scanner (a); scanning itinerary within the study area (b); resulted MLS point cloud (c).

3. RESULTS AND DISCUSSIONS

3.1 UAS PPK data processing

Using the Teobox PPK tool (v. 0.5.6), for each image, the antenna offset parameters relative to the camera lens were calculated and assigned to the camera optical center position. The solution of the carrier based relative positioning and the integer ambiguity was properly resolved, with the solution being 100% fixed in both flights.
The skyplot of the visible satellites during the flights shows that in the oblique flight, 16 satellites were tracked, including 10 from the GPS constellation and 6 from GLONASS, the elevation mask being set to 10 degrees. During the nadiral flight, 15 satellites were tracked, including 8 from the GPS constellation and 7 from

[2] https://geospatial.trimble.com/products-and-solutions/trimble-mx9/

GLONASS. These results suggest that there were sufficient visible satellites for accurate data processing during both flights. Figure 6 shows the correlation between the number of visible satellites and the Dilution of Precision (DOP) values, including the geometric DOP (GDOP), position DOP (PDOP), horizontal DOP (HDOP), and vertical DOP (VDOP). As expected, an increase in the number of satellites leads to an improvement in each individual DOP, while a decrease in the number of satellites results in an increase in all DOP values. Additionally, the DOP values in this study fall within the excellent to ideal range. Overall, this information suggests that the data collected during the flights was of high quality and suitable for further analysis.

3.2 Teodrone UAV image processing

The collected images were processed with *Reality Capture*[3] exploiting the PPK information (Section 3.2.1) or an indirect georeferencing approach (Section 3.2.2). In both cases, the images were oriented through a Bundle Block Adjustment (BBA) with additional parameters (focal length, principal point, radial and tangential distortion).

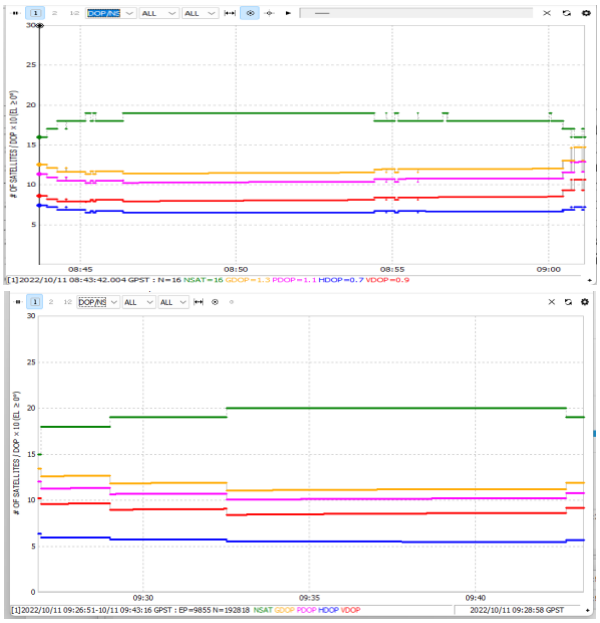

Figure 6. The DOPs values in the case of the 60 m oblique flight (a) and 60 m nadir flight (b) as visualised in Teobox PPK tool.

3.2.1 Teodrone image processing with PPK-based CoP

The a-priori horizontal accuracy of the PPK-based CoP was given by the Teobox PPK tool and loaded to Reality Capture, resulting in a mean value of 7.2 cm a-priori accuracy for the nadiral flight, and 4.7 cm for the oblique flight. Each GCP was manually measured on each image as they appeared. For both datasets, the number of GCPs varied, from 0 to 10, resulting in 11 scenarios. The root mean square errors (RMSE) on Check Points (ChPs) are reported, for the oblique and nadir flights in Table 1 and 2, respectively. The residuals are given in cm and in relation with the average GSD of the nadir flight (1.9 cm).
Figure 7 shows cameras, GCPs and ChPs geolocation with color-coded accuracy for the best scenario: PPK processing with no GCP for the oblique flight and PPK processing with 2 GCPs for the nadiral flight.

60 m OBLIQUE FLIGHT					
No. GCPs	$RMSE_X$ (cm and pixel)	$RMSE_Y$ (cm and pixel)	$RMSE_Z$ (cm and pixel)	$RMSE_{X,Y}$ (cm and pixel)	$RMSE_{Tot}$ (cm and pixel)
0	1.7/0.5	1.6/0.5	1.8/0.6	2.3/0.7	2.9/0.9
1	1.7/0.5	1.6/0.5	2.0/0.6	2.3/0.7	3.1/1.0
2	1.9/0.6	1.8/0.6	2.1/0.7	2.6/0.8	3.4/1.0
3	1.7/0.5	1.8/0.6	2.1/0.7	2.5/0.8	3.2/1.0
4	2.0/0.6	2.1/0.7	2.0/0.6	2.9/0.9	3.5/1.1
5	2.0/0.6	1.7/0.5	2.1/0.7	2.6/0.8	3.4/1.0
6	1.6/0.5	1.6/0.5	2.0/0.6	2.3/0.7	3.0/0.9
7	1.6/0.5	1.6/0.5	1.8/0.6	2.3/0.7	2.9/0.9
8	1.7/0.5	1.6/0.5	1.7/0.5	2.3/0.7	2.9/0.9
9	1.7/0.5	1.6/0.5	1.7/0.5	2.3/0.7	2.9/0.9
10	1.7/0.5	1.6/0.5	1.8/0.6	2.3/0.7	2.9/0.9

Table 1. Residuals (in cm and pixel) calculated for 84 ChPs in the oblique flight with known PPK COPs and a varying number of GCPs.

60 m NADIR FLIGHT					
No. GCPs	$RMSE_X$ (cm and pixel)	$RMSE_Y$ (cm and pixel)	$RMSE_Z$ (cm and pixel)	$RMSE_{X,Y}$ (cm and pixel)	$RMSE_{Tot}$ (cm and pixel)
0	6.7/3.4	6.7/3.4	97/49	9.6/4.8	98/50
1	3.3/1.7	5.8/3.0	5.8/3.0	6.7/3.4	8.8/4.5
2	2.0/1.0	2.3/1.2	1.8/0.9	3.0/1.6	3.5/1.8
3	1.8/0.9	2.4/1.2	1.8/0.9	3.0/1.5	3.5/1.8
4	2.2/1.1	2.4/1.2	1.8/0.9	3.3/1.7	3.7/1.9
5	1.9/1.0	1.7/0.9	1.9/1.0	2.5/1.3	3.2/1.6
6	1.8/0.9	1.7/0.9	2.0/1.0	2.5/1.3	3.2/1.6
7	1.9/1.0	1.7/0.9	1.9/1.0	2.5/1.3	3.2/1.6
8	1.9/1.0	1.6/0.8	1.9/1.0	2.5/1.3	3.1/1.6
9	1.9/1.0	1.6/0.8	1.9/1.0	2.5/1.3	3.1/1.6
10	2.0/1.0	1.6/0.8	1.9/1.0	2.6/1.3	3.2/1.6

Table 2. Residuals (in cm and pixel) calculated for 84 ChPs in the nadir flight with known PPK COPs and a varying number of GCPs.

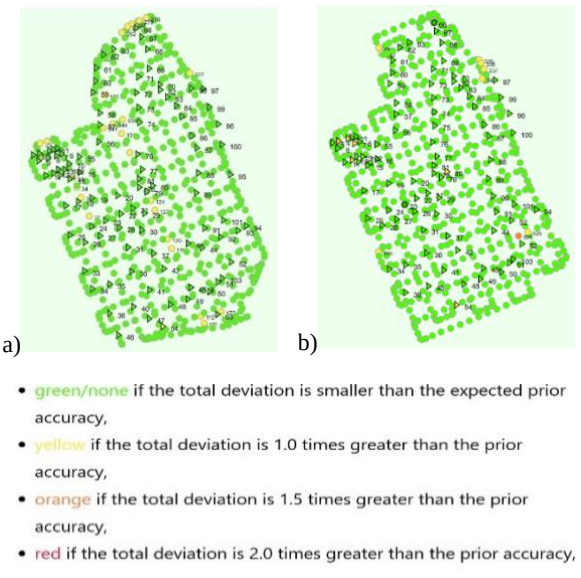

Figure 7. Cameras (dots) and GCPs and ChPs geolocations (triangles) represented in color-coded with respect to the achieved accuracy for the oblique (a) and nadir (b) flight.

In addition, the histograms in Figure 8 show the number of cameras (Y-axis) whose total 3D deviation to the prior accuracy

[3] https://www.capturingreality.com/realitycapture

from the *flight log* file is within values on the X-axis. Histogram bins are colored as described in the legend presented in Figure 7 with the accuracy threshold set to 0.08 m for the oblique flight (Figure 8a) and 0.13 m for the nadiral flight (Figure 8b).

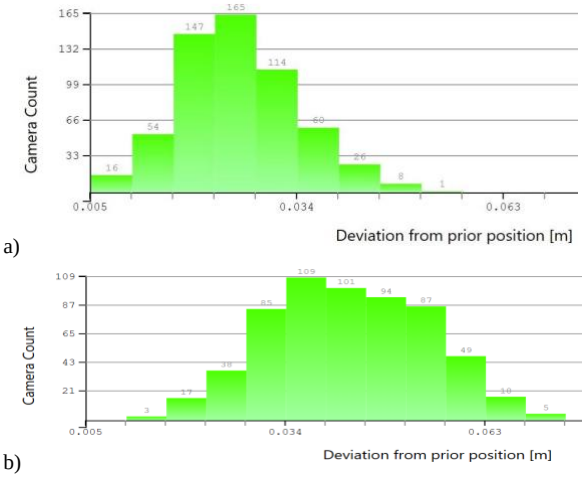

Figure 8. Histogram for the oblique (a) and nadir (b) flight and 2 GCPs: number of cameras whose spatial deviation to the prior accuracy is within values shown on the x axis.

The planimetric errors ($RMSE_{X,Y}$) are 2-3 cm for the oblique flight and 3 cm for the nadir flight, except for the scenarios of nadir flight with 1 GCP and none GCP, for which an error of 1 dm is obtained. The vertical errors ($RMSE_Z$) in the case of the oblique flight are about 2 cm, while the total errors ($RMSE_{Tot}$) are around 3 cm. Analysing the nadir flight, when no GCP is used, the vertical error is 1 m, decreasing to 5.8 cm when introducing one GCP as constraint in the BBA. Using 2 and up to 10 GCPs, the vertical error decreases to about 2 cm with a total error of about 3.5 cm. Notably, increasing the number of GCPs from 3 to 10 only improved the errors by a few millimetres. The trend of $RMSE_{Tot}$ varying the number of GCPs is reported in Figure 9 for the nadir flight and in Figure 10 for the oblique flight. To double-check Reality Capture results, Agisoft Metashape was also employed, showing comparable results for all the oblique and nadir flight scenarios, a part for the nadir flight with zero GCPs. In fact, while Metashape shows a $RMSE_{Tot}$ of 15.8 cm, Reality Capture $RMSE_{Tot}$ is 98.2 cm. Analysing the vertical RMSE of each GCP appears that they have all the same sign, and almost the same entity, as it was a constant translation error. A similar behaviour was found by Benassi et al. (2017). In both software three radial and two tangential distortion parameters have been used. If in Metashape also affinity distortion is added for the nadir flight, an RMSE of 1.6/1.9/3.9 cm is reached for the three directions. These results will be further investigated in a future work, also analysing other flights carried out in the same study area. In the case of the oblique flight (Figure 10), it is worth noting how more than 2-3 GCPs do not increase the accuracy respect the case study of zero GCPs. These results show that is feasible to use only the PPK COP positions to georeferenced the photogrammetric model with a camera network robust enough. The nadiral scenario have to be further investigated with more tests and analyses.

3.2.2 Teodrone image processing for indirect georeferencing

For both datasets, following Oniga et al. (2020), we evaluated the effect of the number and distribution of GCPs in indirect georeferencing and aerial triangulation. 84 points are used as ChPs, while the other 10 have been divided into subgroups to obtain 8 different scenarios (Figure 11).

In the first scenario, which used the minimum number of GCPs (three), we placed one GCP in the center of the study area (point 23), one on the north side of the area (point 66), and one on the southwest side of the area (point 46).

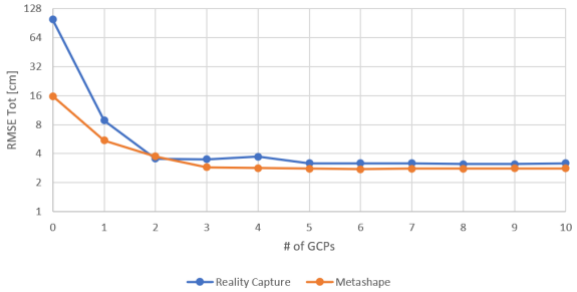

Figure 9. Variation of $RMSE_{Tot}$ in the nadir flight while changing the number of GCPs: Reality Capture in blue and Agisoft Metashape in orange.

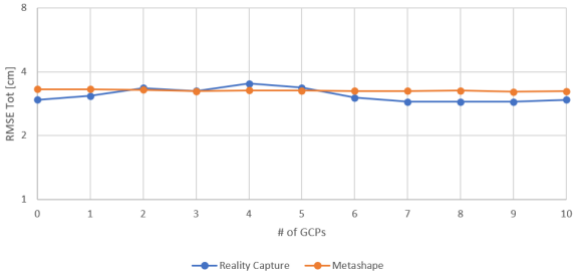

Figure 10. Variation of $RMSE_{Tot}$ in the oblique flight, while changing the number of GCPs: Reality Capture in blue and Agisoft Metashape in orange.

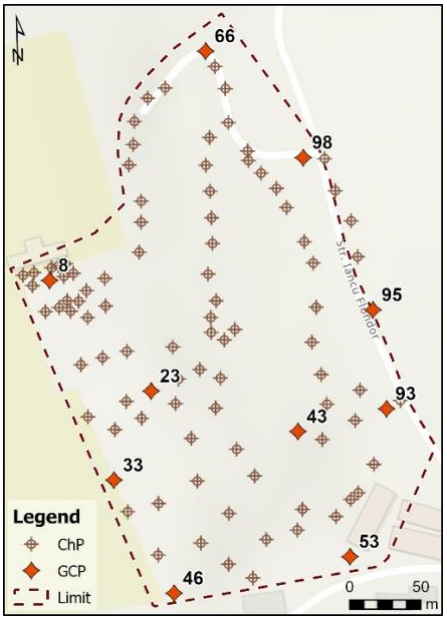

Figure 11. The spatial distribution of the 10 GCPs and 84 ChPs.

For the second scenario, we added a new GCP on the east edge of the study area (point 95), and for the third scenario, we introduced a new GCP on the northwest edge of the study area (point 8). In the fourth scenario, we added a new GCP on the southeast edge of the study area (point 53). In the fifth scenario, we placed a new GCP in the center of the study area (point 43).

For the remaining three scenarios, we added GCPs on the edges of the study area. The RMSEs on 84 ChPs is reported in Table 3 and Table 4 for the oblique and nadir flight, respectively.
The planimetric values ($RMSE_{X,Y}$) ranged between 2.5–3.8 cm for the oblique flight and between 2.8-8.9 cm for the nadir flight, with the highest error corresponding to the minimum of GCPs scenario. In the case of the nadir flight, looking at the first two scenarios, we can see that the errors are two times larger in the case of the nadiral flight, which is to be expected. Therefore, a minimum number of 5 well distributed GCPs on the edges and in the middle are essential to limit the horizontal error. The improvement for the oblique flight is less marked. It is noteworthy that starting with the fourth scenario, the planimetric errors between the oblique and nadiral flights are only a few millimetres apart.
The vertical errors ($RMSE_Z$) varied for the oblique flight between 1.7-11.7 cm, while for the nadir flight, they were between 4.1-65.9 cm, with the highest error occurring in the three-GCPs scenario in both cases.
Regarding $RMSE_{Tot}$, there is a significant improvement in accuracy for the oblique flight when using four GCPs instead of three (from 12.3 to 4.1 cm). However, for the following scenarios, the accuracy does not improve by more than 1 cm. For the nadir flight, five GCPs achieved an accuracy of 5.8 cm, and subsequent scenarios only showed an improvement of at most 1 cm. As expected, the values are better for the oblique flight, than for the nadir flight, especially when the minimum number of GCPs is used.

60 m OBLIQUE FLIGHT					
No. GCPs	$RMSE_X$ (cm and pixel)	$RMSE_Y$ (cm and pixel)	$RMSE_Z$ (cm and pixel)	$RMSE_{X,Y}$ (cm and pixel)	$RMSE_{Tot}$ (cm and pixel)
3	1.9/0.6	3.3/1.0	11.7/3.6	3.8/1.2	12.3/3.8
4	1.6/0.5	2.6/0.8	2.7/0.8	3.1/0.9	4.1/1.3
5	1.8/0.6	1.9/0.6	2.6/0.8	2.6/0.8	3.7/1.1
6	1.7/0.5	2.0/0.6	2.1/0.7	2.6/0.8	3.4/1.0
7	1.7/0.5	2.0/0.6	1.8/0.6	2.6/0.8	3.2/1.0
8	1.7/0.5	1.9/0.6	1.8/0.6	2.5/0.8	3.1/1.0
9	1.7/0.5	1.8/0.6	1.7/0.5	2.5/0.8	3.0/0.9
10	1.7/0.5	1.8/0.6	1.7/0.5	2.5/0.8	3.0/0.9

Table 3. Residuals calculated for 84 ChPs using a different number of GCPs for indirect georeferencing in the oblique flight.

60 m NADIR FLIGHT					
No. GCPs	$RMSE_X$ (cm and pixel)	$RMSE_Y$ (cm and pixel)	$RMSE_Z$ (cm and pixel)	$RMSE_{X,Y}$ (cm and pixel)	$RMSE_{Tot}$ (cm and pixel)
3	8.1/4.1	3.6/1.8	65/33.6	8.9/4.5	66/33.9
4	4.3/2.2	5.4/2.8	4.7/2.4	6.9/3.5	8.4/4.3
5	3.0/1.5	2.4/1.2	4.4/2.2	3.8/2.0	5.8/3.0
6	2.7/1.4	2.1/1.1	4.1/2.1	3.4/1.7	5.3/2.7
7	2.3/1.2	2.0/1.0	4.4/2.2	3.0/1.6	5.4/2.7
8	2.2/1.1	1.8/0.9	4.1/2.1	2.8/1.5	5.0/2.5
9	2.1/1.1	1.8/0.9	4.1/2.1	2.8/1.4	4.9/2.5
10	2.1/1.1	1.8/0.9	4.1/2.1	2.8/1.4	4.9/2.5

Table 4. Residuals calculated for 84 ChPs using a different number of GCPs for indirect georeferencing in the nadir flight.

3.2.3 Quality assessment of the cadastral boundaries extracted from the UAS orthophotos

An orthophoto of the study area for each dataset was generated at 1.3 cm/px and 1.0 cm/px resolution for the oblique and nadir flight, respectively.
Using the orthophotos, the cadastral boundaries such as natural and artificial fences and the roads (Crommelinck et al., 2017), were manually digitized in AutoCAD Map 3D (Figure 12a). The same cadastral features were manually extracted by drawing polylines directly on the MLS point cloud in the Cyclone from Leica Geosystem (Figure 12b). The digitized features were superimposed and a visual analysis was made, checking if they overlap correctly (Figure 13). From Figure 13 we can see that in some areas the cadastral details could not be digitized because of trees. Furthermore, it can be noticed a distance ranging from 1 cm to 30 cm between the elements extracted from the orthophoto and those from the MLS point cloud.

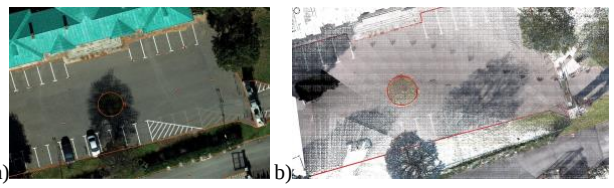
a) b)

Figure 12. Cadastral details digitized on the orthophoto (a) and in the MLS point cloud (b).

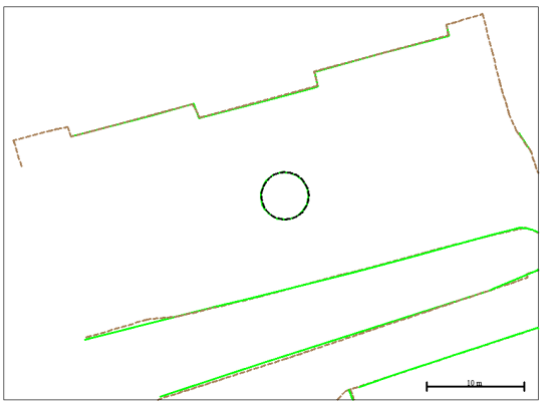

Figure 13. Superimposed cadastral details digitized in the orthophoto (green continuous line) and in the MLS point cloud (brown dashed line).

If the surveyed area was free of vegetation or other obstacles, the digitization in the MLS point cloud is performed very quickly and easily (Figure 14a). However, it is important to acknowledge its limitations, as data can only be acquired along roads, which can be sparsely distributed in rural areas, resulting in a partial reconstruction of the survey area. Additionally, dense foliage along the roadways presents a challenge in extracting the necessary information, such as the cadastral boundary materialized by a fence (Figure 14b-c). Furthermore, the high cost associated with using mobile laser scanning technology compared to drone surveying must also be considered.

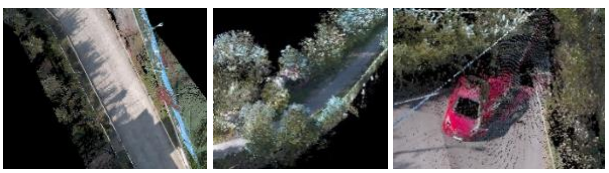
(a) (b) (c)

Figure 14. Different areas from MLS point cloud to be digitized: easy to interpret (a), difficult to digitize the cadastral details (b), (c).

3.2.4 Quality assessment of the UAS point clouds with respect to MLS point cloud

The best UAS scenarios (i.e PPK processing with 0 GCP for the oblique flight and PPK processing with 2 GCP for the nadir flight – Table 1-2) were further processed by generating a dense point cloud. From the results, roads and parking lots were manually

extracted and compared with the MLS point cloud using the M3C2 (Multiscale Model to Model Cloud Comparison) distances implemented in CloudCompare (Lague et al., 2013). As shown in Figure 13, a standard deviation of 5 cm for the oblique UAS point cloud and of 6 cm for the nadir UAS point cloud were achieved.

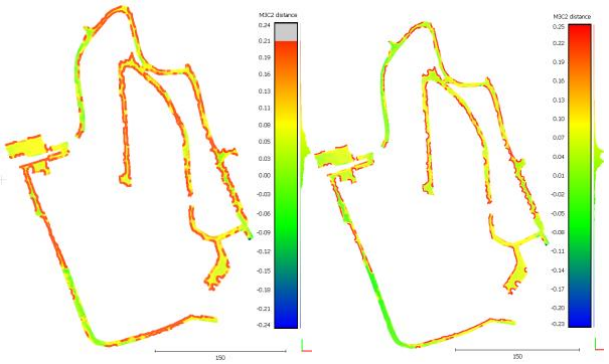

(a) (b)

Figure 15. UAS point clouds coloured based on M3C2 distances from the MLS point cloud: oblique (a) and nadir (b) flights.

4. CONCLUSIONS

The present study evaluates the performances of an improved low-cost UAS system (DJI Phantom 4 Pro v2) coupled with the TeoKIT. Specifically, we analyzed the accuracy of the GNSS-aided georeferencing in PPK mode without the use of GCPs and with an increasing number of GCPs from 1 to 10, in comparison to the classical indirect georeferencing approach. Our results show that a photogrammetric block with oblique images and GNSS coordinates processed in PPK mode without the use of GCPs yields an RMSE accuracy of 2.9 cm (total error vector) on 84 check points, while for the nadir block, the RMSE accuracy reached 3.5 cm when using 2 GCPs. Comparing the generated UAS point clouds with the available MLS data, an absolute accuracy of approximately 5 cm was achieved. However, we note that the MLS technology is limited in residential areas by the need to survey from roads that are usually not well distributed over the territory, as well as having a view angle from the ground that is much more limited in this scenario than from an aerial flight.

ACKNOWLEDGMENTS

The work was supported by a grant of the Ministry of Research, Innovation and Digitization, CNCS-UEFISCDI, project number PN-III-P1-1.1-TE-2021-1185, within PNCDI III.

REFERENCES

Benassi, F., Dall'Asta, E., Diotri, F., Forlani, G., Morra di Cella, U., Roncella, R. and Santise, M., 2017. Testing accuracy and repeatability of UAV blocks oriented with GNSS-supported aerial triangulation. *Remote Sensing*, *9*(2), p.172.

Crommelinck, S., Bennett, R., Gerke, M., Yang, M.Y., Vosselman, G., 2017. Contour Detection for UAV-Based Cadastral Mapping. *Remote Sens.*, *9*, 171.

Cucci, D.A., Rehak, M. and Skaloud, J., 2017. Bundle adjustment with raw inertial observations in UAV applications. *ISPRS Journal of photogrammetry and remote sensing*, *130*, pp.1-12.

Dragomir, P.I., Rus, T., Avramiuc, N., Dumitru, P., 2011. EVRF2007 as Realization of the European Vertical Reference System (EVRS) in Romania. *RevCAD–J. Geod. Cadastre*, 11, 51–63.

Girardeau-Montaut, D., 2014. CloudCompare. http://www.danielgm.net/index.php

Ekaso, D., Nex, F. and Kerle, N., 2020. Accuracy assessment of real-time kinematics (RTK) measurements on unmanned aerial vehicles (UAV) for direct geo-referencing. *Geo-spatial information science*, *23*(2), pp.165-181.

Forlani, G., Pinto, L., Roncella, R. and Pagliari, D., 2014. Terrestrial photogrammetry without ground control points. *Earth Science Informatics*, 7, pp.71-81.

Granshaw, S.I., 2016. Photogrammetric terminology. *The Photogrammetric Record*, *31*(154), pp.210-252.

Hugenholtz, C., Brown, O., Walker, J., Barchyn, T., Nesbit, P., Kucharczyk, M. and Myshak, S., 2016. Spatial accuracy of UAV-derived orthoimagery and topography: Comparing photogrammetric models processed with direct geo-referencing and ground control points. *Geomatica*, *70*(1), pp.21-30.

Ioli, F., Pinto, L. and Ferrario, F., 2021. Low-cost DGPS Assisted Aerial Triangulation for sub-decimetric accuracy with non-RTK UAVs. *International Archives of the Photogrammetry, Remote Sensing and Spatial Information Sciences*, *43*, pp.25-32.

Jaud, M., Bertin, S., Beauverger, M., Augereau, E., Delacourt, C., 2020. RTK GNSS-assisted terrestrial SfM photogrammetry without GCP: Application to coastal morphodynamics monitoring. *Remote Sensing*, 12(11), p. 1889.

Lague, D., Brodu, N., Leroux, J., 2013. Accurate 3D comparison of complex topography with terrestrial laser scanner: Application to the Rangitikei canyon (N-Z). *ISPRS Journal of Photogrammetry and Remote Sensing*, 82, pp.10-26.

Micheletti, N., Chandler, J.H., Lane, S.N., Clarke, L.E., Nieldr, J.M, 2015. Structure from Motion (SfM) Photogrammetry. *Geomorphological Techniques*: London, UK.

Morelli, L., Menna, F., Vitti, A. and Remondino, F., 2022. Action Cams and Low-Cost Multi-Frequency Antennas for GNSS Assisted Photogrammetric Applications Without Ground Control Points. *International Archives of the Photogrammetry, Remote Sensing and Spatial Information Sciences*, *48*, pp.171-176.

Nesbit, P.R., Hubbard, S.M. and Hugenholtz, C.H., 2022. Direct georeferencing UAV-SfM in high-relief topography: Accuracy assessment and alternative ground control strategies along steep inaccessible rock slopes. *Remote Sensing*, 14(3), p.490.

Negru, S.A., Geragersian, P., Petrunin, I., Zolotas, A., Grech, R., 2023. GNSS/INS/VO fusion using Gated Recurrent Unit in GNSS denied environments. In *AIAA SCITECH 2023 Forum*, p. 2226.

Nesbit, P.R., Hubbard, S.M. and Hugenholtz, C.H., 2022. Direct georeferencing UAV-SfM in high-relief topography: Accuracy assessment and alternative ground control strategies along steep inaccessible rock slopes. *Remote Sensing*, *14*(3), p.490.

Oniga, E., Breaban, A-I., Pfeifer, N., Chirilă, C., 2020. Determining the Suitable Number of Ground Control Points for UAS Images Georeferencing by Varying Number and Spatial Distribution, *Remote Sensing*.

Pargieła, K., 2023. Optimising UAV Data Acquisition and Processing for Photogrammetry: A Review. *Geomatics and Environmental Engineering*, *17*(3), pp.29-59.

RealityCapture software— Available online: https://www.capturingreality.com/

Šafář, V., Potůčková, M., Karas, J., Tlustý, J., Štefanová, E., Jančovič, M., Cígler Žofková, D., 2021. The Use of UAV in Cadastral Mapping of the Czech Republic. *ISPRS Int. J. Geo-Inf. 10*, 380.

Stöcker, C., Nex, F., Koeva, M. and Gerke, M., 2017. Quality assessment of combined IMU/GNSS data for direct georeferencing in the context of UAV-based mapping. *The International Archives of Photogrammetry, Remote Sensing and Spatial Information Sciences*, *42*, p.355.

Teobox software — Available online: http://sklep.teokit.eu/1_10_teobox-software.html

TeoKIT— Available online: https://teokit.com/. https://fly.teofly.com/app/.

Teppati Losè, L., Chiabrando, F. and Giulio Tonolo, F., 2020. Boosting the timeliness of UAV large scale mapping. Direct georeferencing approaches: Operational strategies and best practices. *ISPRS International Journal of Geo-Information*, *9*(10), p.578.

Tomaštík, J., Mokroš, M., Surový, P., Grznárová, A. and Merganič, J., 2019. UAV RTK/PPK method—an optimal solution for mapping inaccessible forested areas?. *Remote sensing*, *11*(6), p.721.

Xiang, H. and Tian, L., 2011. Method for automatic georeferencing aerial remote sensing (RS) images from an unmanned aerial vehicle (UAV) platform. *Biosystems Engineering*, *108*(2), pp.104-113.

Zeybek, M., 2021. Accuracy assessment of direct georeferencing UAV images with onboard global navigation satellite system and comparison of CORS/RTK surveying methods. *Measurement Science and Technology*, *32*(6), p.0654.